

Unsteady Forced Motion of the Thermal Throat in a Low-Mach Dual-Mode Ramjet Nozzle

Frédéric Olivon^{*†}, Jean-Étienne Durand^{*}, Aurelien Genot^{*} and Estelle Piot^{*}

^{*}DMPE, ONERA, Université Paris Saclay, F-91123 Palaiseau - France

^{*}ONERA/DMPE, Université de Toulouse, F-31055 Toulouse - France

frederic.olivon@onera.fr

[†]Corresponding author

Abstract

The interactions between acoustics waves and the thermal throat in a simplified low-Mach dual-mode ramjet chamber are numerically investigated. The present study aims to understand the thermal throat function in the combustion instabilities observed in such engines. In this context, the ramjet nozzle is thermally choked due to the combustion, here modelled by a steady and imposed heat release distribution. A harmonic inlet velocity forcing is applied to analyze the motion of the thermal throat subjected to an acoustic field. Various amplitudes (1 %-50 % of the steady inlet velocity) and frequencies (50 Hz-1000 Hz) are explored. An empirical and mono-harmonic model is then proposed to describe this relationship between acoustics and thermal throat motion. The numerical simulations and the model results are then compared and limitations are highlighted.

Nomenclature

Latin Letters

A	cross-sectional area [m ²]
x	axial coordinate [m]
y	transverse coordinate [m]
C_p	specific heat at constant pressure [J kg ⁻¹ K ⁻¹]
f	frequency [Hz]
h_t	specific total enthalpy [J kg ⁻¹]
\dot{m}	mass flow rate [kg s ⁻¹]
P	pressure [Pa]
P_v	volumetric power [W m ⁻³]
q	specific heat release distribution [J kg ⁻¹]
q_{tot}	total specific heat addition [J kg ⁻¹]
T	temperature [K]
t	time [s]
u	axial velocity [m s ⁻¹]
v_{iht}	thermal throat axial motion [m s ⁻¹]
D_0	Damköhler number
M	Mach number
St	Strouhal number

Greek Letters

Δx	axial mesh size [m]
δx	characteristic length [m]
Δy	transverse mesh size [m]
η	imposed velocity amplitude
γ	isentropic coefficient
ϕ	phase shift [rad]
τ	time delay [s]

Superscripts

\cdot'	fluctuating part of a quantity
$\hat{\cdot}$	fast Fourier transform
$\bar{\cdot}$	mean part of a quantity
\cdot^*	non-dimensional quantity
$\bar{\cdot}$	steady or unperturbed quantity

Subscripts

1	combustion chamber position
i	inlet flow
t	total quantity
tht	quantity at the thermal throat

UNSTEADY FORCED MOTION OF A THERMAL THROAT

1. Introduction

A dual-mode ramjet can operate in both subsonic and supersonic combustion processes, covering a wide range of flight Mach numbers suitable for the new hypersonic vehicles [1, 2]. Although a geometrically choked nozzle is sufficient for ramjet operations during which the combustion is subsonic in the chamber (Fig. 1a), this technology is not appropriate for scramjet operation characterised by supersonic combustion (Fig. 1b). In contrast, the thermally choked ramjet [3, 4] (Fig. 1c), generated by the heat of combustion, requires only a divergent duct, allowing a smooth transition from subsonic to supersonic combustion. However, this requires optimal flow and combustion control in the dual-mode ramjet.

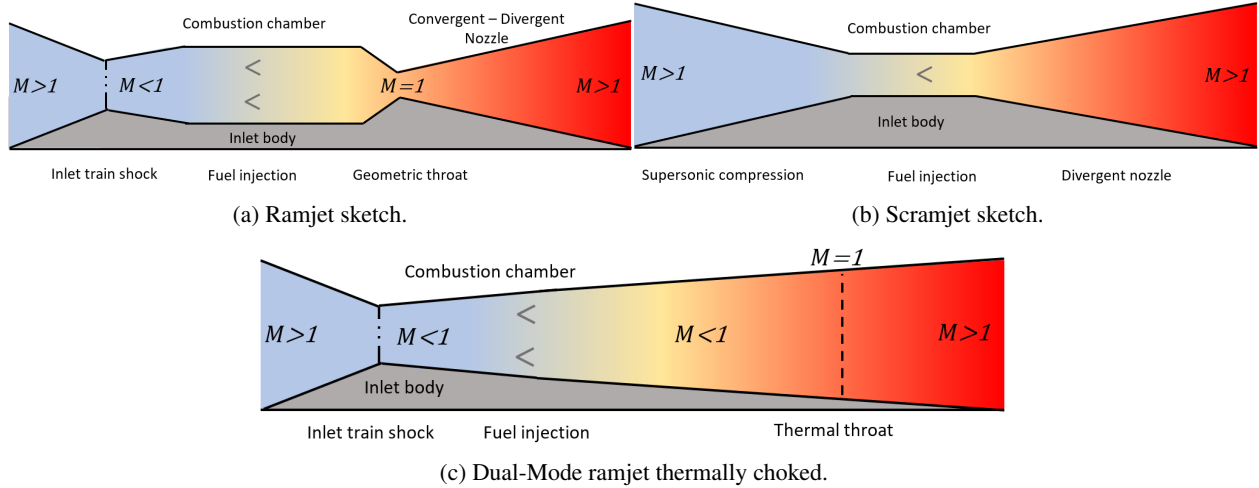


Figure 1: Sketch of various airbreathing engines: 1a) Ramjet sketch with geometric throat; 1b) Scramjet sketch; 1c) Dual-mode ramjet sketch with thermal throat.

Under particular operating conditions, the ramjets, scramjets or dual-mode ramjets are prone to combustion instabilities, leading to pressure oscillations, combustion chamber extinction, flashback, or even causing significant damages on the engine [5, 6, 7]. To design a dual-mode ramjet with a thermal throat, the acoustic-flame-hydrodynamic coupling, causing these combustion instabilities, needs to be defined and understood. As a first step, this paper is focused on the acoustic field in a generic dual-mode ramjet involving a thermal throat (located where the Mach number is equal to 1).

Very few studies are focused on the characterization of the acoustic field considering a thermal throat as an acoustic boundary. Particularly, Lin *et al.* [8] have led pioneering work in this topic by considering the combustion dynamics and the thermal throat as a unique compact source bounding the acoustic domain downstream (Fig. 2a). The flame and the thermal throat position are thereby assumed identical. Three acoustic feedback loops are then described, occurring between the upstream shock, the fuel injection and the flame-thermal throat. However, the authors have focused their work on studying the frequency of these feedback loops without acoustically characterising the boundary conditions formed by the thermal throat.

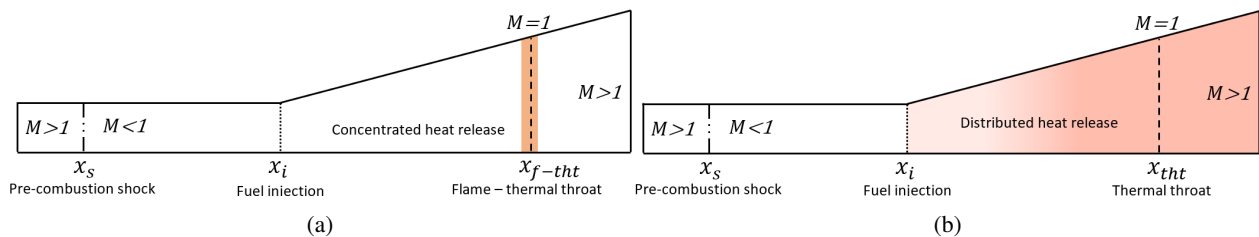


Figure 2: Sketch of two combustion approaches: 2a) Compact combustion zone as described by Lin *et al.* [8]; 2b) Distributed combustion zone approach used in this paper.

Nonetheless, the knowledge of the dynamics of the thermal throat position and the related response to acoustic perturbations is required to study the acoustic domain of such an engine. In a ramjet configuration, the combustion flames are widely dispersed [9], leading to invalidate the assumption of the compactness of the thermal throat and flame position. In the present study, the choice is made to consider a distributed combustion zone, see Fig. 2b. Thus, the thermal throat

freely positions itself in the flame heat release.

Section 2 details the methodology, assumptions, and numerical parameters used in this study. Numerical parameters are justified in section 3. In section 4, an empirical model of the unsteady thermal throat response is described and the comparison between CFD and the empirical model is analyzed and discussed. Finally, some conclusions are summarised in section 5.

2. Methodology

To study and characterize the response of the thermal throat in a distributed combustion zone, unsteady velocity fluctuations representative of acoustic waves are emitted from the subsonic flow upstream of the thermal throat, the latter being generated by a heat distribution in a divergent nozzle. To do so, computational fluid dynamics (CFD) simulations based on Euler equations are used.

2.1 Numerical set-up

To facilitate the interpretation of the phenomena involved, the divergent geometry (illustrated in Fig. 2b), which is the simplest way to allow the thermal throat to exist in a duct, is chosen. The geometry investigated in the present study is a two-dimensional domain of total length $L = 2.4$ m and inlet height $y_i = 25$ mm (Fig. 3). It consists of three parts: the air intake ($L_1 = 1$ m, *i.e.* $x_1 \approx 0.42L$), the combustion chamber ($L_2 = 0.4$ m, *i.e.* $x_2 \approx 0.58L$) and the nozzle ($L_3 = 1$ m, *i.e.* $x_L = L$) [4]. The middle part avoids the diffraction of acoustic waves as shown by Jou and Menon [10, 11] thanks to a gradually increasing angle between the area of constant cross-section and the diverging channel. The steady combustion q is imposed from x_1 to x_L , in the cross-section variation zone.

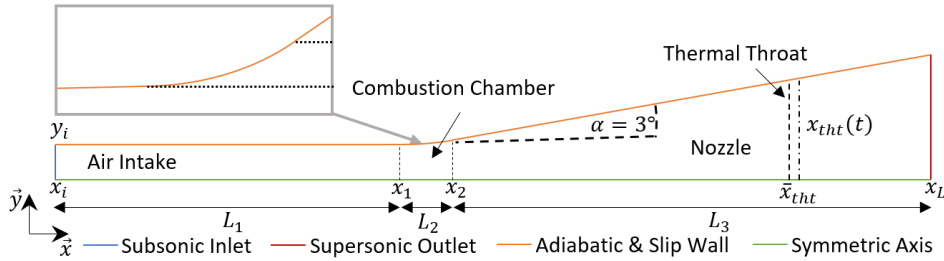


Figure 3: Sketch of the computational domain.

In a dual-mode ramjet, the flame and the heat release are highly impacted by acoustic perturbations, leading to a coupling between the thermal throat response with direct acoustic perturbations and heat release modifications of the flame. To capture the variations of the thermal throat position due to acoustic perturbations only, combustion is set up as steady, *i.e.* the heat added to the flow by the combustion is imposed as a steady distribution becoming insensitive to the acoustic perturbations. Hence, the steady combustion is numerically added along the combustion chamber and the nozzle by a heat release model q (defined in section 2.2), such as shown in Eq. (1).

$$h_t(x) = h_{t,i} + q(x) \quad (1)$$

By this decoupling, the analysis and the characterization of the variation of the thermal throat position induced by upstream acoustic perturbations, called the thermal throat position response, are therefore possible.

At the inlet, an acoustic forcing is added to the mean boundary condition (with more details in subsection 2.3). Adapted to acoustic studies [12, 13], Euler flow equations are chosen as a first approach to avoid the complexity induced by the presence of wall boundary layers and thermodiffusive phenomena. This simplification should ease the understanding of the relationship between the dynamics of the core-flow and that of the unsteady thermal throat.

The volumetric power P_v is used as an Eulerian source term, implemented in the CFD code, and inferred with equation (3) from the mass flow rate conservation:

$$P_v = \frac{\dot{m}_i}{A} \frac{dq}{dx} \quad (2)$$

UNSTEADY FORCED MOTION OF A THERMAL THROAT

with $\dot{m}_i = \rho_i u_i A_i$ calculated from isentropic relations and the Table 1, and q modeled by Eq. (3) (built by the algorithm defined in subsection 2.2).

The numerical simulations are performed with the ONERA CFD code CEDRE [14]. The non-reactive 2D Euler equations are solved. Air is injected at the inlet boundary x_i . The heat capacity C_p is computed with an eight-order polynomial function in local static temperature. Spatial discretization is performed by a second-order multi-slope MUSCL scheme [15] and an HLLC flux scheme [16]. Time integration is performed by an implicit second-order Runge-Kutta scheme [17, 18].

2.2 One-dimensional steady heat release model

To establish a thermal throat, a steady one-dimensional heat distribution q has to be defined (see Eq. (1)). This added energy in the flow plays the role of a steady flame giving a certain amount of energy to the system. In the constant cross-section area, the flow is not heated, and $q(x)$ is equal to zero. In the divergent, the form of the function chosen for the imposed heat addition is described by the equation (3). This form is inspired by the results of the study of Wang *et al.* [2].

$$q(x, \sigma) = \begin{cases} 0 & \forall x \in [x_i, x_1] \\ q_{tot} \frac{1 - e^{-(x-x_1)^2/(2\sigma)}}{1 - e^{-(x_L-x_1)^2/(2\sigma)}} & \forall x \in [x_1, x_L] \end{cases} \quad (3)$$

where σ denotes the width factor and $q_{tot} = D_0 C_{p,i} T_{t,i}$ is the total specific heat added to the nozzle with D_0 the Damköhler number.

To determine q_{tot} and σ , a specific algorithm is developed (Fig.4). The specific heat capacity C_p is assumed constant along the entire nozzle and equal to its inlet value $C_{p,i}$. This facilitates the resolution of the algorithm.

All the following steps, illustrated in Fig. 4, are done for a target thermal throat position x_{tht} . First, D_0 is guessed, giving the total added specific heat q_{tot} . Then, to determine σ , the local thermal throat equation, described by Zierep [19] and Heiser and Pratt [20], is used:

$$\frac{1}{A} \frac{dA}{dx} \Big|_{x_{tht}} = \frac{1}{C_p T} \frac{dq}{dx} \Big|_{x_{tht}} \quad (4)$$

with A the local cross-sectional area.

To determine the Mach number evolution, the standard following equation is used [21]:

$$\frac{1}{M} \frac{dM}{dx} = \frac{-1}{1-M^2} \left[\left(1 + \frac{\gamma-1}{2} M^2 \right) \frac{1}{A} \frac{dA}{dx} - \frac{1+\gamma M^2}{2C_p T} \frac{dq}{dx} \right] \quad (5)$$

As the Mach number is equal to $M = 1$ at the thermal throat position x_{tht} , a first-order backward discretization gives the inlet Mach number M_{i-D_0} . If the inlet Mach number M_{i-D_0} is equal to the chosen one M_i (Tab. 1), the guessed Damköhler number D_0 is appropriate. Otherwise, another Damköhler number D_0 has to be chosen and the previous steps are repeated.

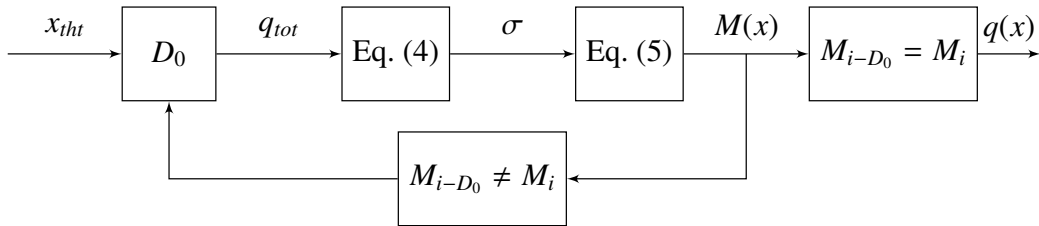


Figure 4: Algorithm to define the steady heat release axial.

This algorithm then provides a model for q which will be used in the source term of the Euler simulations (see Eq.(2)). It provides also a 1D-distribution of Mach number which can be compared to the results of the Euler simulations.

2.3 Steady boundary conditions, heat release parameters and inlet acoustic forcing

The steady inlet conditions are given in Table 1, coherent with the operating conditions found in the literature [4, 22]. As sketched in Figure 3, slip-adiabatic boundary conditions are imposed on the upper nozzle wall meanwhile having a symmetry boundary condition for the lower segment. The outlet is supersonic.

Table 1: Inlet conditions.

M_i - Mach Number	$T_{t,i}$ - Total Temperature	P_i - Static Pressure	$C_{p,i}$ - Heat Capacity	
Value	0.6	600 K	2×10^5 Pa	$1043 \text{ J kg}^{-1} \text{ K}^{-1}$

The thermal-throat target is chosen as $x_{tht}/L = 0.80$. So, the algorithm defined in subsection 2.2 gives the following constants for the heat release function q (Eq. (3)):

$$q_{tot} = 1.91 \text{ MJ kg}^{-1} \quad \sigma = 0.30 \quad (6)$$

The resulting function is plotted in Figure 5. The added volumetric power $P_v(x)$ (defined in Eq. (2) with $P_{v,max} = 508 \text{ MJ s}^{-1} \text{ kg}^{-1}$) is also drawn. The heat release function $q(x)$ is monotonically increasing, while the power $P_v(x)$ reaches a maximum close to $x/L \approx 0.6$.

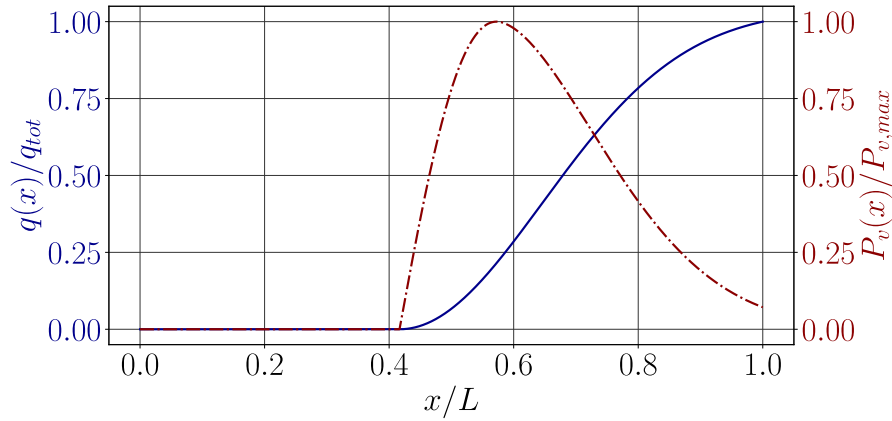


Figure 5: Specific heat addition $q(x)$ (blue line) and volumetric power $P_v(x)$ (red dashed line).

To characterize the response of the thermal throat to imposed disturbances from the inlet, sinusoidal velocity oscillations are imposed at the inlet (x_i in Fig. 3), simulating acoustic motions induced by the unsteady combustion in a real combustion chamber [23]. Inlet velocity perturbations are described by:

$$u(x = x_i, t) = \bar{u}_i(1 + \eta \sin(2\pi f_i t)) = \bar{u}_i + u'_i(t) \quad (7)$$

with \bar{u}_i the steady inlet velocity, u'_i the acoustic forcing, η the imposed inlet velocity relative amplitude and f_i the imposed inlet frequency.

The frequency range was established on the basis of the main longitudinal and transverse acoustic modes. The lowest longitudinal acoustic frequency can be estimated with $f_0 = c_0/(2l)$, where c_0 is the sound velocity in the nozzle and l is the chosen length. The thermal throat can move between $l = x_1$ and $l = x_L$, thus this frequency ranges between $f_{0,long} = 100 \text{ Hz} - 250 \text{ Hz}$. In addition, the cut-on range of the transverse acoustic modes can be estimated with $l = 25 \text{ mm} - 88 \text{ mm}$, yielding to the cut-on frequency $f_{0,trans} = 4650 \text{ Hz} - 9430 \text{ Hz}$. Consequently, the simulations will be performed with a frequency between $50 \text{ Hz} - 1000 \text{ Hz}$ to study only longitudinal modes. For the velocity amplitude range, it has been set up to $0.01 - 0.50$ of the steady inlet velocity as performed by Oh *et al.* [23]. It should be stressed that this range of amplitude leads to velocity fluctuations that greatly exceed the range of validity of linear acoustics theory.

As these ranges are scanned by 19 f_i -values and 11 values of η , the present parametric study covers more than 200 operational conditions, providing a broad view of the thermal throat response.

3. Numerical convergence

3.1 Numerical parameters

A three-part structured grid mesh is used with a constant cell size of $\Delta x_1 = 500 \mu\text{m}$ in the L_1 section, while in the pre-thermal throat part (x_1 to x_{tht}), the cells are refined until $\Delta x_{tht} = 50 \mu\text{m}$ and then stretched again to Δx_1 in the post-thermal throat region (x_{tht} to x_L). This non-constant spatial discretization allows a smaller mesh size while keeping a satisfactory resolution.

The time step is set up to $\delta t_{CFD} = 1 \times 10^{-6}$ s for the CFD simulations. The inlet velocity law is updated every ten CFD time steps *i.e.* $\delta t_{LAW} = 1 \times 10^{-5}$ s. As the entire flow field is stored for post-processing (PP), in order to minimize the memory and time load, it was decided to modulate the temporal resolution of the PP based on the inlet forcing frequency. In this approach, each time period is divided into twenty equidistant sub-intervals, as shown in Eq. (8), ensuring consistent precision across different frequencies and enabling accurate Fast Fourier Transform (FFT) analysis [24] according to the Shannon criterion.

$$\delta t_{PP}(f_0) = \frac{1}{20f_0} \quad (8)$$

3.1.1 Mesh independence study

The possible influence of spatial resolution is first investigated by varying the mesh size. The impact of mesh refinement is evaluated on the static temperature and pressure terms which are the main thermodynamic quantities of interest. Five computational grids have been studied. The thermal throat mesh size is varied from $\Delta x_{tht} = 200 \mu\text{m}$ (362 000 cells data) to $\Delta x_{tht} = 25 \mu\text{m}$ (842 000 cells data). Simulations are performed with a CFD time step $\delta t_{CFD} = 1 \times 10^{-7}$ s. To have roughly rectangular cells along the nozzle, the constant transverse mesh size is set up to $\Delta y = \Delta x_i/2$.

Figure 6 shows the maximum relative errors (ε_{max}) versus the number of cells in the mesh grid, for static pressure and temperature. This criterion allows us to have a precise overview of the errors between two meshes. The mesh being non-constant along the nozzle length, the grid size refers to the x -axis cell size at the thermal throat position. Maximum relative error ε_{max} is calculated with equation (9). This error compares the values between a loose mesh χ_g and a fine mesh χ_f . Each mesh is then compared in pairs.

$$\varepsilon_{max}(\chi) = \left| \frac{\chi_g - \chi_f}{\chi_f} \right| \quad (9)$$

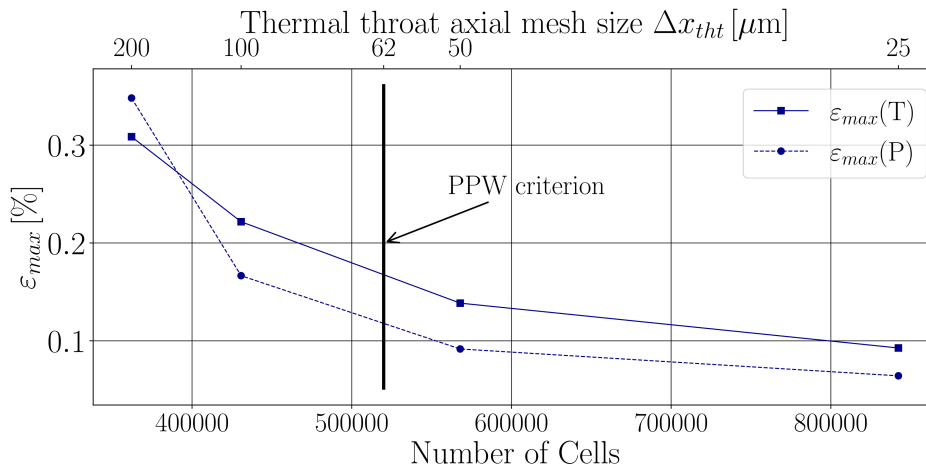


Figure 6: Maximal relative error versus the mesh refinement, for static pressure $\varepsilon_{max}(P)$ and temperature $\varepsilon_{max}(T)$.

One can see that the maximal relative errors on both the static temperature and the pressure are very low ($< 0.4\%$), even for the coarser mesh, which proves that mesh convergence is verified even with that one. However, as this study is unsteady, the thermal throat is moving: the mesh refinement has to be able to capture this motion accurately enough.

Moreover, the mesh must be fine enough so that the acoustic wave propagation is captured without significant numerical dissipation or dispersion effects.

As described by Langenais *et al.* [25, 26] and Haider [27], with the chosen spatial and time schemes, the required number of mesh cells in a characteristic length is at least $PPW = 20$. The characteristic length δx_{tht} of the thermal throat oscillation can be estimated with equation (10).

$$\delta x_{tht} = \frac{\bar{u}(x_{tht})\eta}{2\pi f_i} ; \Delta x = \frac{\delta x}{PPW} \quad (10)$$

According to the range of the acoustic forcing parameters, the most demanding case is $(\eta, f_i) = (0.01, 1000 \text{ Hz})$. This yields a minimum characteristic length $\delta x_{tht} = 1.2 \text{ mm}$ and a minimum mesh size of $\Delta x_{tht} = 62 \text{ mm}$ at the thermal throat position. As the inlet mesh size Δx_i is not a sizing parameter for the motion of the thermal throat, it is set at $\Delta x_i = 10\Delta x_{tht}$ to reduce the total mesh size.

Due to the low computational cost of such a 2D grid, we choose to be even more conservative and the axial mesh size is set up to $\Delta x_i = 500 \text{ }\mu\text{m}$ and $\Delta x_{tht} = 50 \text{ }\mu\text{m}$, which leads to a total mesh size of 567 000 cells.

3.1.2 Steady thermal throat position

The simulation of the steady flow of an air mixture heated by an added volumetric power set-up as explained in section 2.2 is now presented. The numerical parameters are the ones selected in the previous sections. The thermal throat position is computed in the steady case, *i.e.* without any forcing at the inlet.

Figure 7 shows the Mach number distribution given by the Euler simulation. The transverse variation of the flow field is very small, which validates the 1D assumption used for the heat release model (Sec. 2.2). The steady thermal

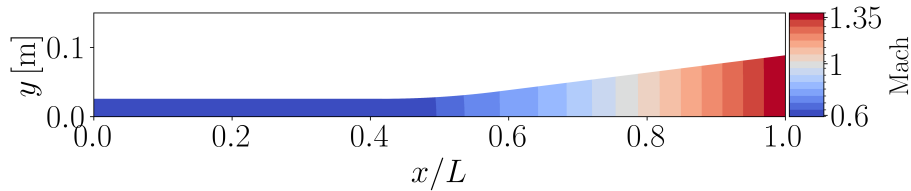


Figure 7: Mach field in the nozzle with a thermal throat.

throat is located at $x_{tht,CFD}/L = 0.78$, while the targeted position by the algorithm is $x_{tht,1D}/L = 0.80$. This small discrepancy is certainly due to the assumption of constant heat capacity C_p (equal to $C_{p,i}$) made in the model of section 2.2. In the following, the position obtained by CFD will be used as a reference, *i.e.* $\bar{x}_{tht} = 1.86 \text{ m}$.

3.2 Time convergence: thermal throat motion, under acoustic forcing at the inlet

The influence of the temporal resolution is now investigated by varying the CFD time step δt_{CFD} . Four time steps are tested from $\delta t_{CFD} = 1 \times 10^{-7} \text{ s}$ to $\delta t_{CFD} = 5 \times 10^{-6} \text{ s}$. The mesh is the one selected in the previous section, and a forced CFD simulation is run with the most demanding operating conditions with regards to the capture of the thermal throat motion, *i.e.* $(\eta, f_i) = (0.01, 1000 \text{ Hz})$.

Figure 8 shows that the motions of the thermal throat position are identical for $\delta t_{CFD} \leq 1 \times 10^{-6} \text{ s}$, so this time step value is selected for the CFD simulations.

UNSTEADY FORCED MOTION OF A THERMAL THROAT

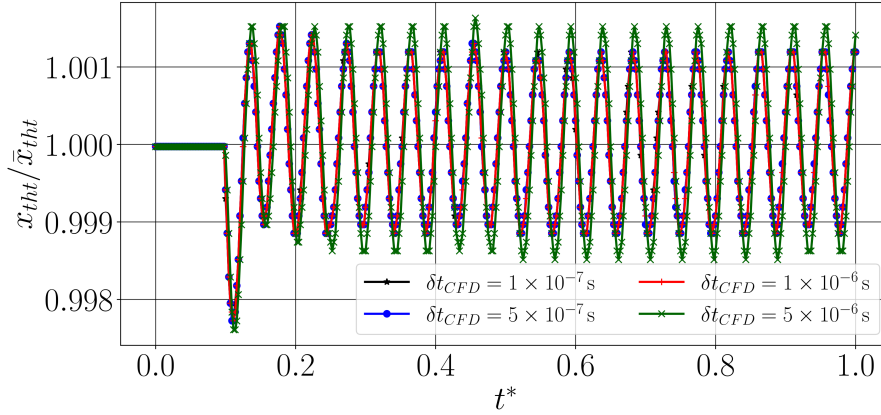


Figure 8: Reduced thermal throat response for various CFD time steps δt_{CFD} , at the inlet conditions: $(\eta, f_i) = (0.01, 1000 \text{ Hz})$.

4. Discussion and results

4.1 Thermal throat motion: determination of an *ad-hoc* empirical model

Several authors have examined the motion of boundary conditions in ramjet and scramjet configurations, such as inlet shock trains or flame. For instance, Oh *et al.* [23] have investigated the unsteady position of the inlet shock train, which was induced by downstream acoustic perturbations. By using models proposed by Culick and Rogers [28], the authors established a connection between downstream acoustic waves and shock motion. This model, applicable for small acoustic amplitudes, is based on the unsteady motion of the shock due to acoustic disturbances and on shock relations. This study played a pioneering role in characterizing the acoustic boundary conditions in ramjet engines.

A similar approach is used here. The motion of the thermal throat is inherently affected by fluctuations. In the current study, the following assumptions are made: (i) the dynamics of the thermal throat is only influenced by the periodic velocity forcing at the inlet; (ii) the mean position response \tilde{x}_{tht} differs from the steady position \bar{x}_{tht} and the two are related by the equation $\tilde{x}_{tht} = \beta \bar{x}_{tht}$; (iii) transient phenomena, such as acoustic time travel or thermal throat inertia, are represented by a time lag τ ; (iv) the speed of the thermal throat motion can be expressed as:

$$v_{tht}(t) = \frac{d}{dt} x_{tht}(t) = \alpha u'_{tht}(t + \tau) = \alpha \eta \bar{u}_{tht} \sin(2\pi f_i(t + \tau)) \quad (11)$$

with α a coefficient related to the local velocity forcing and τ the time delay between the inlet velocity forcing and the effective thermal throat velocity forcing. \bar{u}_{tht} refers to the flow velocity at the steady thermal throat position, u'_{tht} to the corresponding velocity fluctuations.

A priori, all coefficients α , β and τ are functions of both the amplitude η and frequency f_i of the velocity forcing at the inlet (defined in Eq. (7)). By integrating the equation (11), the position of the thermal throat writes:

$$\begin{aligned} x_{tht}(t) &= \tilde{x}_{tht} + \int v_{tht}(t) dt \\ &= \beta \bar{x}_{tht} + \int \alpha \eta \bar{u}_{tht} \sin(2\pi f_i(t + \tau)) dt \\ &= \beta \bar{x}_{tht} + \alpha \eta \bar{u}_{tht} \int \sin(2\pi f_i(t + \tau)) dt \\ &= \beta \bar{x}_{tht} - \frac{\alpha \eta \bar{u}_{tht}}{2\pi f_i} \cos(2\pi f_i(t + \tau)) \end{aligned} \quad (12)$$

Following the approach of Klein *et al.* [29], a Strouhal number is introduced and defined by $St = \frac{2\pi f_i \bar{x}_{tht}}{\eta \bar{u}_{tht}}$. Consequently:

$$x_{tht}(t) = \beta \bar{x}_{tht} \left[1 - \frac{\alpha}{\beta St} \cos(2\pi f_i(t + \tau)) \right] \quad (13)$$

A large Strouhal number $St \gg 1$ implies that the thermal throat stays near its mean position $\beta\bar{x}_{th}$. Conversely, for a small Strouhal number $St \ll 1$, the amplitude of the oscillation is large and the thermal throat is strongly affected by the perturbations. The motion of the thermal throat is then amplified.

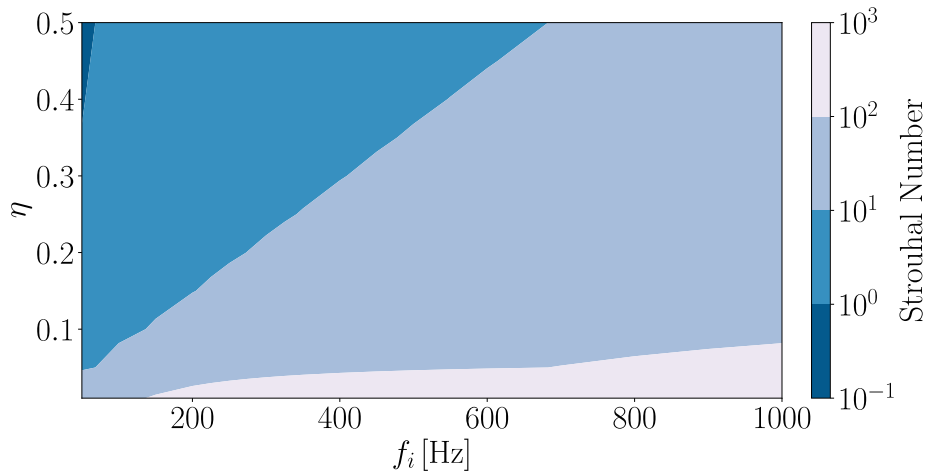


Figure 9: Distribution of the Strouhal number as a function of both inlet frequency and inlet amplitude disturbance.

Figure 9 shows the distribution of the Strouhal number calculated with the model presented section 2.2 versus both frequency and amplitude inlet disturbance. Three Strouhal number zone can be observed. First, in low frequency $f_i < 50$ Hz and high amplitude $\eta > 0.40$, the Strouhal number is low $St < 1$. With this configuration, it is expected that the thermal throat oscillations will be large. Both other Strouhal zones are larger than $St > 1$, even larger than $St > 10$. Thus, main operating conditions should provide a thermal throat response close to the mean position, with low amplitude oscillations. This empirical model assumes that the thermal throat motion has a purely single-frequency response.

4.2 Numerical observation of the thermal throat motions

Figure 10a shows the time-evolution of the thermal throat for the forcing case $(\eta, f_i) = (0.15, 150$ Hz). The thermal throat turns out to exhibit oscillations around a mean value that slightly differs from the position obtained in the steady configuration. The minimal value is close to $x_{th}/\bar{x}_{th} = 0.96$ but the maximal value is $x_{th}/\bar{x}_{th} = 1.03$. Additionally, a small time shift is observed: indicating the time taken for the acoustic waves to travel from the inlet to the thermal throat position. Figure 10b shows the FFT of the aforementioned signal. The fundamental harmonic frequency of the thermal throat position response matches the perturbation frequency at the inlet $f_0 = f_i$. Furthermore, the amplitude of the FFT corresponds to the amplitude of the last ten periods of the thermal throat oscillations. The amplitude of the first harmonic $f_1 = 300$ Hz is here very small, validating the single-frequency assumption for the equation (13).

The thermal throat temporal evolution is shown in Figure 10c for the forcing parameters $(\eta, f_i) = (0.50, 150$ Hz). With an increase in the amplitude of the inlet forcing, the amplitude of the temporal response also increases. However, the thermal throat response is no longer strictly mono-harmonic, exhibiting upper harmonics no longer negligible (a first harmonic amplitude of approximately 35 % of the amplitude of the fundamental f_0 frequency). In addition, an asymmetry of the amplitude from the initial thermal throat position is stated, showing a slower motion upstream than downstream.

From both figures 10a and 10b, the coefficients α , β and τ can be estimated. First, the coefficient β is established from the time-evolution of the signal (Fig. 10a): by taking the ten last oscillations, the mean position \tilde{x}_{th} is measured. Then, $\beta = \tilde{x}_{th}/\bar{x}_{th}$ is calculated. The amplitude coefficient α is determined with the FFT of the signal (Fig. 10b). From the single-frequency assumption, only the amplitude of the fundamental frequency f_0 is taken into account. Then, $\alpha = |\hat{x}_{th}(f_0)|/St$, with St being the Strouhal number of the operating point. The time lag τ is calculated from the time difference between the last oscillation of the thermal throat motion and the last oscillation of the inlet velocity forcing.

UNSTEADY FORCED MOTION OF A THERMAL THROAT

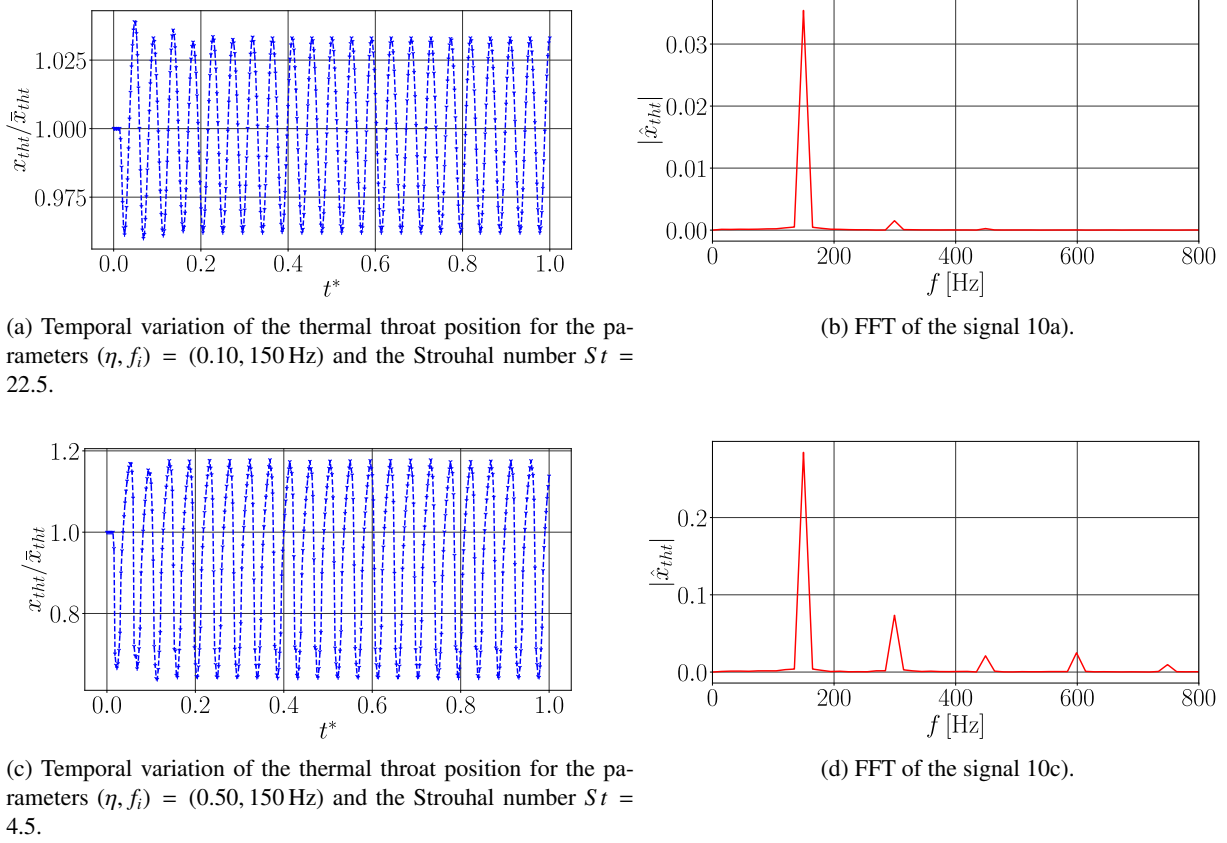


Figure 10: Temporal and frequency response of the thermal throat for two different inlet forcing.

4.3 Behavioural interpretation of the *ad-hoc* model coefficients

In this section, the *ad-hoc* model coefficients are built by comparison between the thermal throat response model presented in section 4.1 and the CFD results, for all operating conditions. Then, the limitations of the model are discussed.

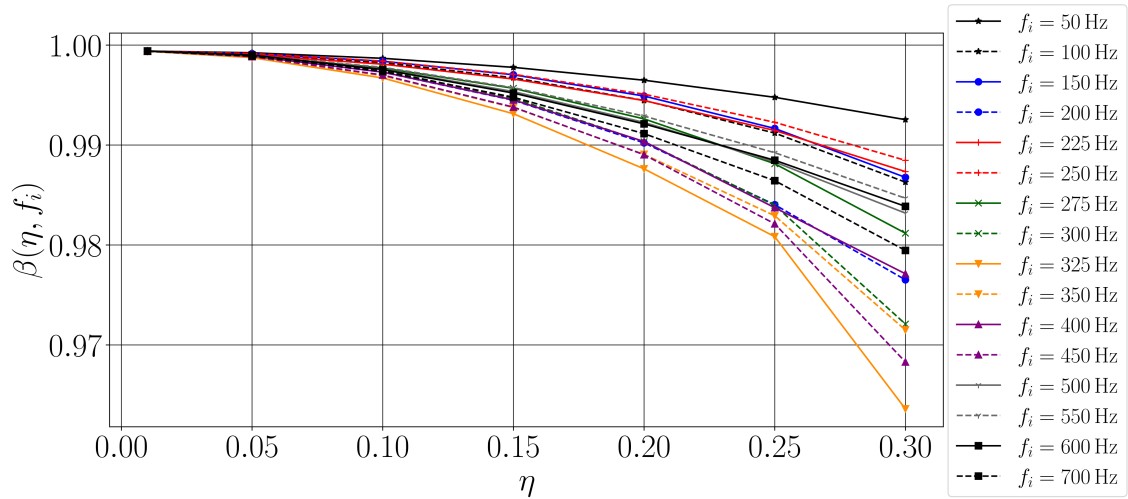
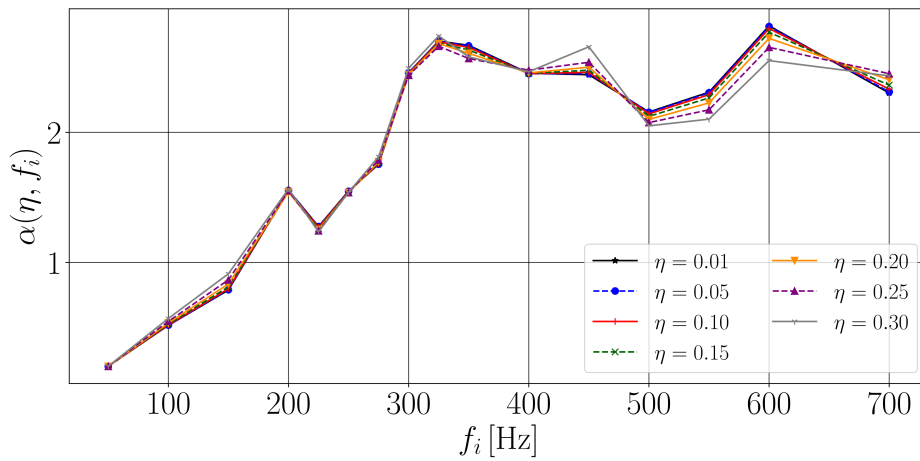
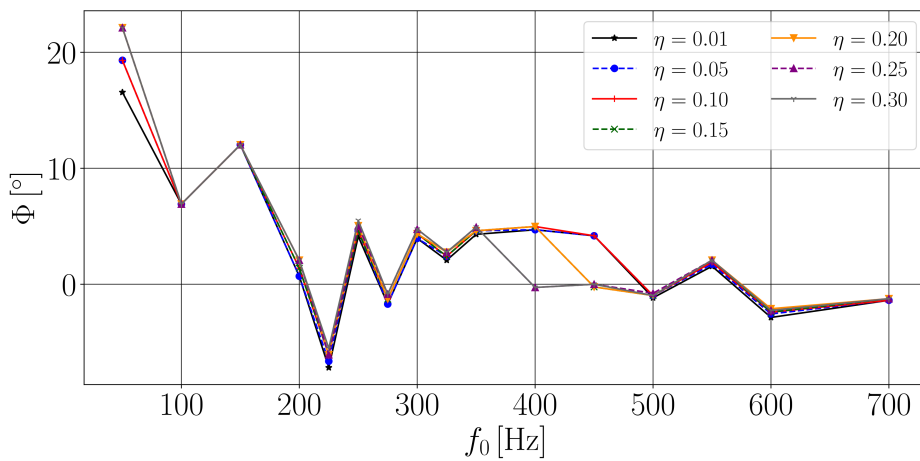
As described previously, the thermal throat position can be described by Eq. (13). CFD simulations are performed with the forcing parameters in the range $[\eta, f_i] \in [0.01, 0.30] \times [50 \text{ Hz}, 700 \text{ Hz}]$, which matches a Strouhal number St range of 2 – 1000. To be able to reconstruct the thermal throat position response, three quantities have to be characterized: α , β and τ .

Figure 11 shows the evolution of the β quantity over the inlet forcing amplitude. For small inlet forcing amplitude, the mean position \tilde{x}_{tht} is close to the steady thermal throat position \bar{x}_{tht} for each case. Then, the more the forcing amplitude η increases, the more important the impact of the forcing frequency f_i is. For high η , the frequencies around $f_i = 300 \text{ Hz}$ are the ones with the largest shift from the steady position.

Figure 12 shows the evolution of the α quantity over frequency for several inlet forcing amplitudes. Two phases can be observed: for small frequencies, the amplitude seems to increase linearly from $f_i = 50 \text{ Hz}$ to $f_i = 325 \text{ Hz}$. In this part, the forcing amplitude seems to play no role in the reduced oscillation amplitude. Then, the oscillation amplitude reaches a plateau at $f_i = 325 \text{ Hz}$. Above this value, the amplitude of the thermal throat oscillations is more sensitive to the inlet forcing amplitude. From both α and β evolutions, the inlet forcing frequency $f_i = 325 \text{ Hz}$ seems to highlight a maximum response of the system.

Figure 13 shows the phase shift ϕ as a function of the inlet forcing frequency for various inlet forcing amplitudes. The phase shift is determined by the time delay τ between the inlet velocity forcing and the thermal throat response, at its established regime. Then, the relation $\phi = 2\pi f_i \tau$ is used. The time delay, or the phase shift, characterizes two distinct phenomena: the characteristic velocity time propagation and the thermal throat transient response time. The

UNSTEADY FORCED MOTION OF A THERMAL THROAT

Figure 11: Reduced mean position β over inlet velocity amplitude η for various frequencies f_i .Figure 12: Reduced oscillation amplitude α over inlet velocity frequency f_i for various forcing amplitudes η .Figure 13: Phase shift Φ between the inlet velocity perturbation and the thermal throat response.

established phase shift cannot distinguish both times.

UNSTEADY FORCED MOTION OF A THERMAL THROAT

Figure 14 shows the signal reconstructed from the *ad-hoc* empirical model for various operating conditions. The reconstruction is compared with the last oscillation of the CFD signal. For low operating conditions, the single-frequency assumption is very well suited for the thermal throat response. For instance, for $(\eta, f_i) = (0.10, 50 \text{ Hz})$ or $(\eta, f_i) = (0.10, 150 \text{ Hz})$, the model and the CFD response are almost identical.

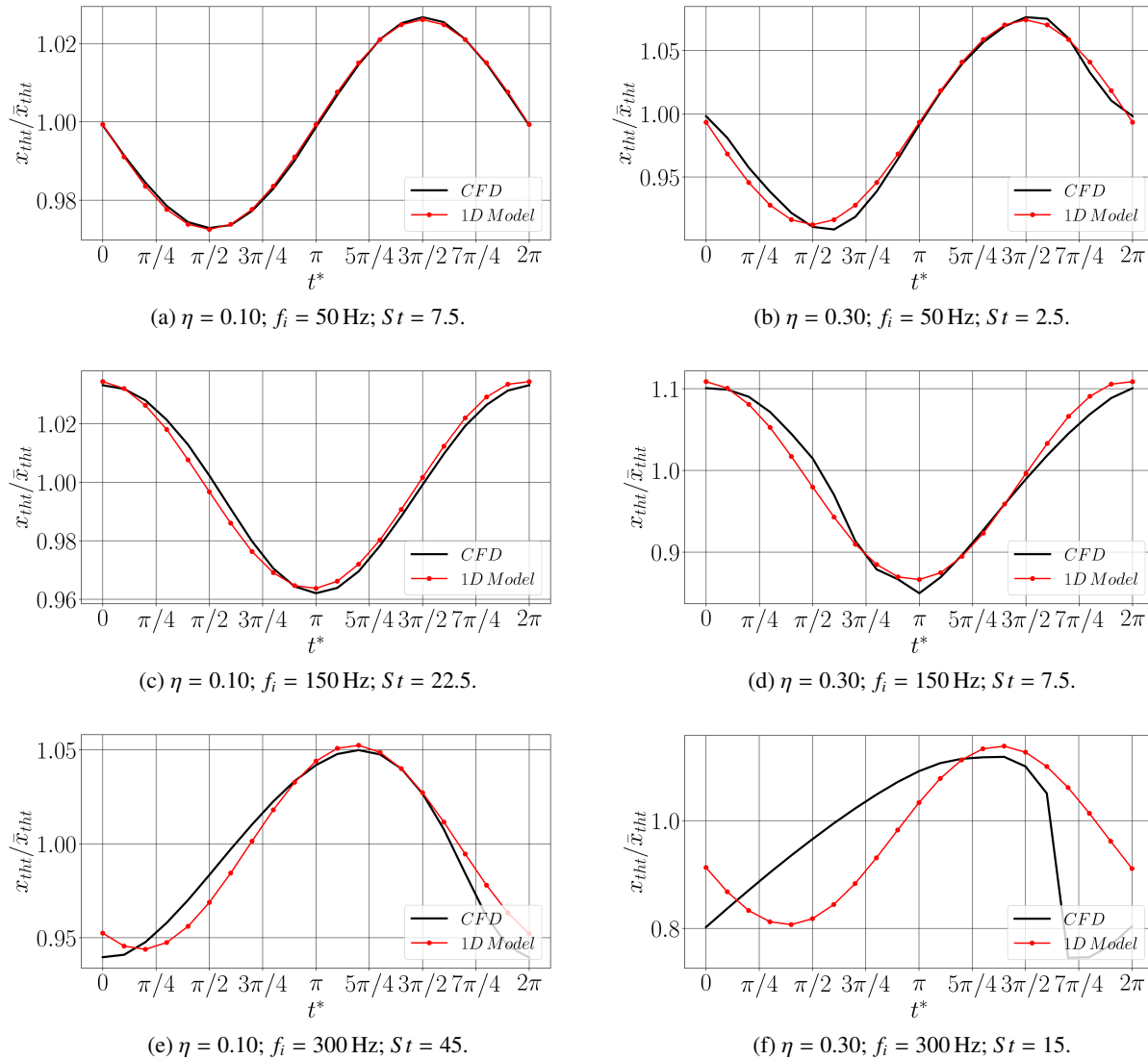


Figure 14: Comparison between CFD and reconstructed signal for various operational conditions (η, f_i) .

However, it is noteworthy that the Strouhal number is not a fully relevant parameter for specifying the thermal throat response. Indeed, while for the case presented in Fig.14a, where the related Strouhal number is equal to $St = 7.5$, the model prediction is very close to the CFD one, for the case presented in Fig.14d, with the same Strouhal number, the empirical model and the CFD response are further apart.

Moreover, other cases invalidate the mono-frequency responses assumption. Especially, in the case $(\eta, f_i) = (0.30, 300 \text{ Hz})$ (Fig.14f), the dynamics of the thermal throat position is not harmonic at all. First, the thermal throat is moving slowly from its upstream to its downstream position. Then, a great shift occurs, pulling back the thermal throat upstream. This behaviour is also observed for frequencies in the range 300 Hz – 700 Hz.

4.4 Model limitations

The range of inlet forcing investigated in the previous section was $\eta < 0.30$ and $f_i < 700$ Hz. Even in this range, the reliability of the mono-harmonic modelling of the thermal throat oscillation response was shown to be limited, *e.g.* for $(\eta, f_i) = (0.30, 300$ Hz) (see Fig. 14f). However, the observed sharp response is still an oscillation of the thermal throat. On the contrary, for $\eta > 0.30$ and $f_i > 700$ Hz, the thermal throat behaviour is strongly different.

Figure 15 shows the evolution of the thermal throat at five successive time steps for $(\eta = 0.50$ and $f_i = 1000$ Hz, illustrated by the Mach-number field. In the first time step, the thermal throat is located at its steady position; then, another thermal throat is formed by the upcoming velocity waves, choking the nozzle locally. This new thermal throat is located at a position where the local condition of the initial thermal throat is no longer verified: the upstream zone is no longer subsonic.

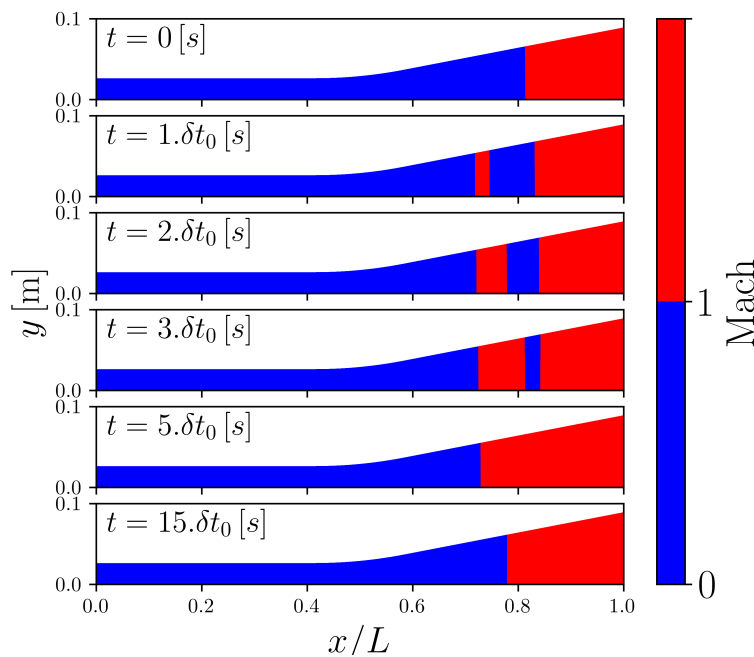


Figure 15: Mach Field of the case $(\eta, f_i) = (0.50, 1000$ Hz), $St = 30$, at six successive time steps ($\delta t_0 = 5 \times 10^{-5}$ s).

The presence of multiple thermal throats causes the post-processing process used for tracking the isoline Mach $M = 1$ to fail. Indeed, the empirical model assumes that only one thermal throat is possible and oscillates around a mean position. When two or more thermal throats are generated in the nozzle, only the upstream thermal throat is captured. This explains the great shift in the thermal throat dynamics.

To summarize all the findings, an overview of the validity of the empirical model of Eq. 13 is presented, using all the data from the numerical parametric study. The model of thermal throat motion assumes a unique thermal throat with a mono-harmonic motion. But, as observed in Figure 10, the spectrum analysis of the throat motion highlights some upper harmonics, which can invalidate the model. This has been confirmed by time analyses in Figures 14f and 15. This overview is illustrated in Figure 16 which shows the validity range of the model of thermal throat motion, based on the numerical parametric study. This map is built by selecting the most upstream thermal throat position and by plotting a criterion based on the ratio between the amplitude of the fundamental frequency and the amplitude of the first upper harmonic of the signal of the thermal throat position: $R = |\hat{x}_{th}(f_1)|/|\hat{x}_{th}(f_0)|$. Operating conditions (η, f_i) lower than the green dashed line $R = 0.10$ means that the model is representative of the thermal throat oscillations. On the contrary, operating conditions higher than the red dashed line $R = 0.20$ means that the mono-frequency assumption and the empirical model are no longer valid. Values between both lines describe operating conditions where the empirical model is not fully satisfied.

Two points need to be pointed out. The first one is a clear dependency of the model validity on the forcing amplitude. The higher the amplitude, the less valid the model is because the harmonics in the thermal throat response are no longer

UNSTEADY FORCED MOTION OF A THERMAL THROAT

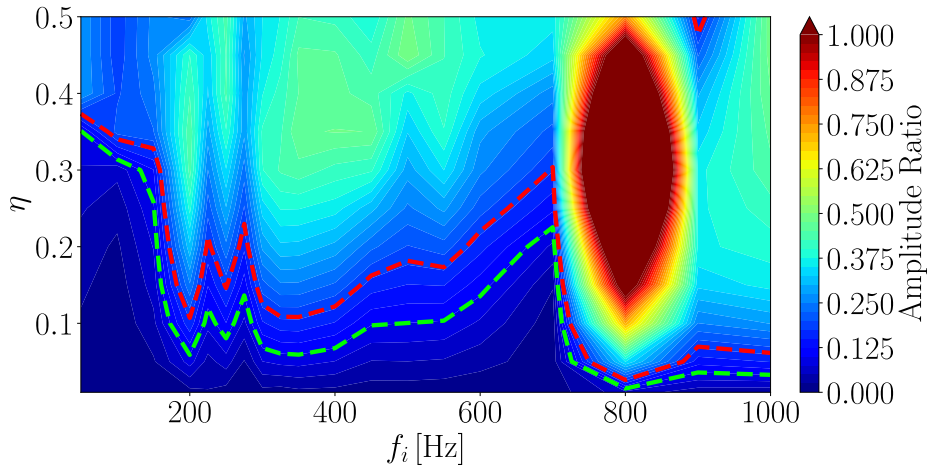


Figure 16: Validity range of our empirical model of thermal throat motion: below the dashed green line: valid; above the dashed red line: invalid

negligible for high amplitudes. Secondly, there is also a clear dependency on the forcing frequency. Its behaviour looks like the α -curves, described in Figure 12, meaning that the geometry responds preferentially to specific frequencies. The validity of the model is particularly critical around $f_i \geq 300$ Hz and above 700 Hz.

5. Conclusion

A generic ramjet with a thermal throat has been modelled numerically by a 2D-Euler simulation with a steady combustion model, proposed in this paper. This numerical ramjet has been acoustically forced to evaluate the thermal throat dynamics. An empirical model of the thermal throat motion, has also been developed, allowing us to improve our understanding of the coupling between acoustic oscillations generated in the combustion chamber and thermal throat dynamics. The proposed model assumes a mono-harmonic motion.

A wide range of forcing frequency (50 Hz – 1000 Hz) and velocity amplitude (0.01 – 0.5) is considered. For low amplitudes, the thermal throat position is oscillating periodically around a mean position, confirmed by the relatively good reproduction of the numerical results by the model. This mean position can slightly be shifted from the steady position, and the more the inlet forcing amplitude increases, the more the mean position moves upstream. The phenomena can be amplified with frequency. For moderate amplitudes, some upper harmonics can be identified in the signal of the thermal throat position, invalidating the model. For higher amplitudes with a sufficiently high frequency ($f_i > 300$ Hz), two thermal throats may appear. The first one is mainly steady. However, the second one propagates along the nozzle until replacing the initial one. Our empirical model is, therefore, no more valid at all.

Other questions remain unclear: the link between the chosen geometry and the preferred response frequency has to be ruled out; moreover further investigations have to be done to understand the thermal throat response around the forcing frequency $f_i = 800$ Hz.

Finally, this study is part of a more global investigation of the thermal throat response to the acoustic field in low-Mach dual-mode ramjet configurations. The acoustic impedance of the thermal throat as well as the unsteadiness interaction remains to be understood and characterized.

6. Acknowledgments

The authors gratefully acknowledge ONERA for its financial support.

References

- [1] F. Falempin. Ramjet and dual mode operation. In *NATO STO EN-AVT-150*, 2008.

- [2] H. Wang, Q. Yang, and X. Xu. Effect of thermal choking on ejection process in a rocket-based combined cycle engine. *Applied Thermal Engineering*, 116:197–204, 2017.
- [3] K. Kato, T. Kanda, K. Kobayashi, K. Kudo, and A. Murakami. Downstream ramjet-mode combustion in a dual-mode scramjet engine. *Journal of Propulsion and Power*, 22(3):511–517, 2006.
- [4] O. Dessornes and D. Scherrer. Tests of the japhar dual mode ramjet engine. *Aerospace Science and Technology*, 9(3):211–221, 2005.
- [5] J.E. Crump, K.C. Schadow, V. Yang, and F.E.C. Culick. Longitudinal combustion instabilities in ramjet engines identification of acoustic modes. *Journal of Propulsion and Power*, 2(2):105–109, 1986.
- [6] A. Roux, S. Reichstadt, N. Bertier, L. Gicquel, F. Vuillot, and T. Poinot. Comparison of numerical methods and combustion models for les of a ramjet. *Comptes Rendus Mécanique*, 337(6):352–361, 2009.
- [7] E. George, V. Sabelnikov, and P. Marge. Self-ignition of ethylene/hydrogen mixtures in unsteady thermal choking conditions: Numerical unsteady RANS investigation. In *WEHSFF 2007 West-East High Speed Flow Field Conference 2007 Moscow*, 2007.
- [8] K-C Lin, K. Jackson, R. Behdadnia, T.A. Jackson, F. Ma, and V. Yang. Acoustic characterization of an ethylene-fueled scramjet combustor with a cavity flameholder. *Journal of Propulsion and Power*, 26(6):1161–1170, 2010.
- [9] W.C.B. Senior, R.M. Gejji, and C.D. Slabaugh. Flame dynamics in an optically accessible solid fuel ramjet combustor. *Journal of Propulsion and Power*, 2023.
- [10] W.-H. Jou and S. Menon. Simulations of ramjet combustor flow fields. II - origin of pressure oscillations. In *19th AIAA, Fluid Dynamics, Plasma Dynamics, and Lasers Conference*. American Institute of Aeronautics and Astronautics, 1987.
- [11] W.-H. Jou and S. Menon. Modes of oscillation in a nonreacting ramjet combustor flow. *Journal of Propulsion and Power*, 6(5):535–543, 1990.
- [12] P. Lojek and A. Golas. Linearized euler equations for the analysis of wave propagation in ducts. In *Forum Acusticum*, page 8 pages, 2020.
- [13] R.S. Goonetilleke, S.G. Lekoudis, and W.C. Strahle. Nonisentropic propagation of sound in uniform ducts using euler equations. *AIAA Journal*, 24(7):1088–1094, 1986.
- [14] A. Refloch, B. Courbet, A. Murrone, P. Villedieu, C. Laurent, P. Gilbank, J. Troyes, L. Tessé, G. Chaineray, J.B. Dargaud, E. Quémerais, and F. Vuillot. CEDRE software. *AerospaceLab Journal*, 2011.
- [15] C. Le Touze, A. Murrone, and H. Guillard. Multislope MUSCL method for general unstructured meshes. *Journal of Computational Physics*, 284:389–418, 2015.
- [16] E. F. Toro, M. Spruce, and W. Speares. Restoration of the contact surface in the HLL-riemann solver. *Shock Waves*, 4(1):25–34, 1994.
- [17] J.C. Butcher. On the implementation of implicit runge-kutta methods. *BIT Numerical Mathematics*, 16(3):237–240, 1976.
- [18] J.C. Butcher. Implicit runge-kutta processes. *Mathematics of Computation*, 18(85):50–64, 1964.
- [19] J. Zierep. Theory of flow in compressible media with heat addition. *AGARD Paris*, 1974.
- [20] W.H. Heiser and D.T. Pratt. *Hypersonic Airbreathing Propulsion*. AIAA education series. American Institute of Aeronautics and Astronautics, 1994.
- [21] F. Bartlmä. *Gasdynamik der Verbrennung*. Springer Vienna, 1975.
- [22] Y.-J. Wang, F. Qin, Z.-Q. Xie, D. Zhang, X.-G. Wei, and G.-Q. He. Experimental research on the thermal throat of rocket based combined cycle combustor. *Applied Thermal Engineering*, 178:115603, 2020.
- [23] J.Y. Oh, F. Ma, S.-Y. Hsieh, and V. Yang. Interactions between shock and acoustic waves in a supersonic inlet diffuser. *Journal of Propulsion and Power*, 21(3):486–495, 2005.
- [24] J.W. Cooley and J.W. Tukey. An algorithm for the machine calculation of complex fourier series. *Mathematics of Computation*, 19(90):297–301, 1965.
- [25] A. Langenais, F. Vuillot, J. Troyes, and H. Lambaré. Computation of the noise radiated by a hot supersonic jet deflected in a flame trench. *The Journal of the Acoustical Society of America*, 149(3):1989–2003, 2021.
- [26] A. Langenais and J. Troyes. Couplage CFD-CAA et propagation non linéaire. In *Couplage CFD-CAA et propagation non linéaire*, 2016.
- [27] F. Haider, B. Courbet, and J.-P. Croisille. A high-order interpolation for the finite volume method: The coupled least squares reconstruction. *Computers & Fluids*, 176:20–39, 2018.
- [28] F.E.C. Culick and T. Rogers. The response of normal shocks in diffusers. *AIAA Journal*, 21(10):1382–1390, 1983.
- [29] J.-M. Klein, A. Gandilhon-Gounelle, A. Vincent-Randonnier, A. Genot, and A. Mura. On the invariance of flame-motion-induced variations of the generalized disturbance energy. *Combustion and Flame*, 251:112711, 2023.